ACS Photonics

Article

pubs.acs.org/journal/apchd5

Flexible Thin-Film InGaAs Photodiode Focal Plane Array

Dejiu Fan,[†,⊥] Kyusang Lee,[†,⊥] and Stephen R. Forrest*[,†,‡,§]

[†]Department of Electrical Engineering and Computer Science, [‡]Department of Physics, and [§]Department of Materials Science and Engineering, University of Michigan, Ann Arbor, Michigan 48109, United States

Supporting Information

ABSTRACT: Natural imaging systems such as the retina and the compound eye employ a conformal architecture that provides an aberration-free image with wide field of view (FOV) and very low *f*/number. However, most artificial imagers such as conventional cameras are limited to a planar architecture demanded by the use of brittle semiconductor focal plane arrays (FPAs). High-resolution image formation on this flat field requires multiple bulky optical elements. Here we demonstrate a general approach to fabricating complex circuits and in particular FPAs on flexible and/or conformable substrates that can be shaped to overcome these fundamental limitations. An 8 × 100, lightweight, thin-film $In_{0.53}Ga_{0.47}As$ p-i-n photodiode FPA with sensitivity to wavelengths as long as λ = 1650 nm is fabricated on a thin flexible plastic foil following transfer by adhesive-free bonding of the epitaxial layers that are subsequently lifted off from the parent InP substrate. The array is shaped into either a convex cylindrically curved imager to achieve a 2π FOV or, when formed into a concave shape, to provide high-resolution and compact spectral decomposition over a wide wavelength range. The array exhibits ∼99% fabrication yield with ∼100% peak external quantum efficiency at λ = 1300 nm. The unique features of this flexible thin-film FPA provide a new paradigm for realizing advanced electronic and imaging applications.

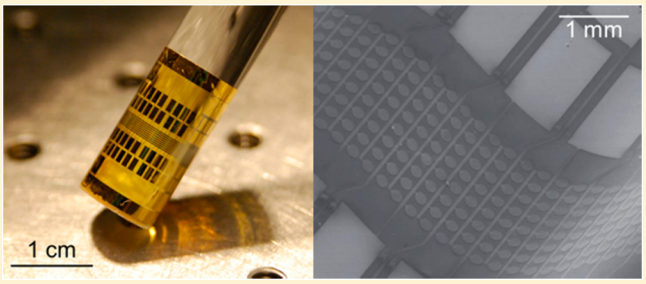

KEYWORDS: *infrared detectors, SWIR, cold-welding, epitaxial lift-off, field of view, spectroscopy*

High-performance photodetector focal plane arrays (FPAs) have been investigated to fulfill the increasing demands for advanced imaging systems. However, the pace of imager development has been primarily limited to planar geometries with their inherent disadvantages, including narrow field of view (FOV) and off-axis optical aberrations.[1,2] The imperfect match between the focal and image planes of simple lenses necessitates additional optical elements[3] that increase the complexity, weight, and cost of the imaging system. Considerable recent efforts[4,5] in the fabrication of flexible electronic devices[2,6−8] has led to demonstration of nonplanar arrays that conform to the focal plane of simple lens system. These demonstrations include deforming the focal plane using semicylindrical[9,10] and hemispherical[11,12] geometries to reduce aberrations and increase the FOV. For example, Song et al.[11] demonstrated conformal photodiode arrays fabricated on stretchable substrates combined with an elastomeric microlens array to achieve an approximately 180° FOV. One shortcoming of that and many similar approaches is the spacing between adjacent detectors is large and often increased on deformation to form nondevelopable three-dimensional curved array surfaces, leading to low-resolution images.

Here, we demonstrate a flexible InGaAs FPA with high optical performance, high yield, and, importantly, high pixel density on a two-dimensional, developable array surface. By sacrificing one dimension of deformation, the pixel spacing remains unchanged upon transforming into the desired conformal shape. It is sensitive across the shortwave infrared (SWIR) spectral range with applications to spectroscopy, night vision, and surveillance. Specifically, we demonstrate the fabrication of a thin-film 8 × 100 InGaAs p-i-n photodiode FPA transferred to a thin plastic foil via cold-weld bonding[13] and then epitaxially lifted off (ELO)[14,15] from its parent (growth) substrate. The FPA is conveniently transformed into a conformal imager owing to the flexibility of the substrate, absence of brittle adhesives, and the very thin semiconductor devices mounted onto its surface. The conformal FPAs are used as a compact, *convex,* 1 cm diameter cylindrical imager that achieves a 360° in-plane FOV; that is, it demonstrates "2π awareness". Moreover, by imparting a *concave* curvature, we demonstrate very high resolution, aberration-free spectral decomposition of multiple wavelengths extending across the SWIR, providing significantly improved performance compared with planar arrays used in conventional spectrophotometric applications. The methods employed can readily be extended to a wide range of devices, from active pixel sensors to light-emitting diodes used in flexible displays.[15] The method is independent of the semiconductor materials choice and can in principal achieve extremely high pixel densities due to the complete elimination of solder-bump technology typically used in bonding detectors to readout back planes.[16−18]

Our FPA, weighing only 30 mg, shows nearly perfect fabrication yield (∼99%) and an external quantum efficiency

Received: January 18, 2016
Published: March 16, 2016

DOI: 10.1021/acsphotonics.6b00042
ACS Photonics 2016, 3, 670−676

(EQE) of ~100% at a wavelength (λ) of 1300 nm, with an almost equally high sensitivity from λ = 980 to 1650 nm. An integrated back side metal mirror reduces the active layer thickness by almost half that of a conventional InGaAs photodiode while maintaining high absorption.[19,20] These results confirm that thin film arrays provide flexibility while maintaining high performance that can exceed analogous substrate-based devices. The unique features of this imaging system enable a broad range of applications, including high-resolution spectroscopy,[21] robotics,[9] and telescopes.[2,22]

RESULTS AND DISCUSSION

Photodiode Characterization. The fabrication process, illustrated in Figure 1, is discussed in detail both previously[13−15] and in the Methods. Figure 2A and B show the thin-film

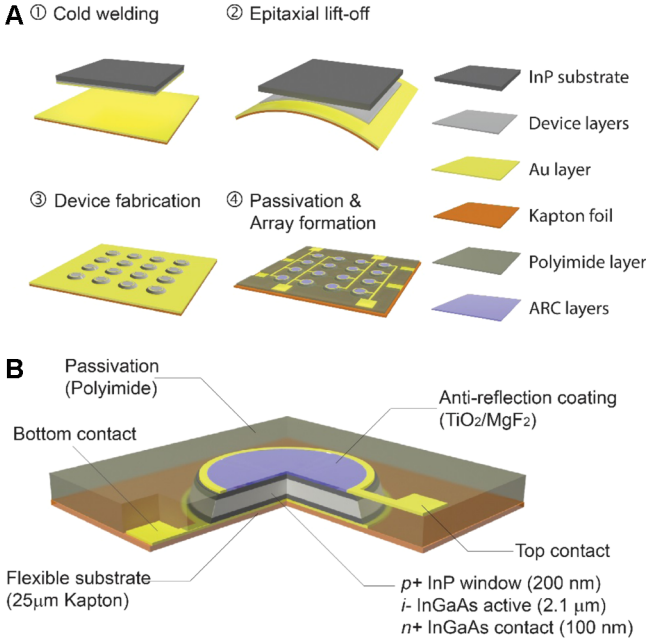

Figure 1. (A) Process flow for fabrication of the thin-film InGaAs p-i-n photodiode array. ① After growth and sample dicing, Ir (0.5 nm)/Au (200 nm) is coated on both the epitaxial surface and the Kapton host substrate. ② The metal films are brought into contact under pressure and slightly elevated temperatures to form a cold-weld bond. This is followed by epitaxial lift-off to remove the substrate from the foil. ③ The top ring anode contact is patterned, and the photodiode mesas are etched. ④ The back side row contacts are patterned; polyimide passivation is applied to the mesa edges and is opened to allow for deposition and pattering of the column contacts, followed by deposition of the antireflection coating in the device top contact rings. (B) Cross sectional view of a photodiode.

8 × 100 InGaAs p-i-n photodiode array bonded to the Kapton foil. The array is ultralightweight (<30 mg) and flexible (bend radius <0.5 cm). The back side Au contact acts as a reflective mirror that enhances the optical absorption due to light interference in the photoactive layer. In principle, 100% peak absorption can be achieved in thin-film devices for any wavelength between 980 and 1650 nm by optimizing the antireflection coating (ARC) and active layer thicknesses. Here, the ARC is designed to maximize the response at λ = 1300 nm while maintaining >85% light transmission between λ = 980 and 1650 nm. Figure 2C shows the calculated optical intensity distribution[23] within the 2.1 μm thick InGaAs i-layer of the device in Figure 1B, compared with that of a substrate-based device with the same structure, clearly illustrating the improved light absorption in the thin-film device. A comparison of EQE at λ = 1550 nm at −1 V for the thin-film devices vs substrate-based devices with different InGaAs absorption layer thicknesses is shown in Figure 2D. The simulated and measured EQE spectra of the thin-film photodiode are indicated by the line and data points in Figure 2E, respectively. The measured EQEs are 82%, 99%, and 88% at λ = 980, 1300, and 1550 nm, respectively. The inset of Figure 2E shows the current−voltage (I−V) characteristics of a 40 μm diameter photodiode under dark and 100 μW laser illumination at λ = 1550 nm. The dark current is 4.0 ± 0.8 nA. To our knowledge, EQE ≈ 100% is the highest reported for InGaAs imagers.[19,20,24−26]

Detector Performance and Reliability. As shown by the histograms in Figure 3A, the yield of the 8 × 100 photodiode array is ~99% (790/800 photodiodes had a leakage current of <1 μA at −1 V). Similar yields were obtained on 10 × 10 photodiode arrays transferred to a Kapton foil (see Supplementary Figures S1 and S2). In that case, the 40 μm diameter detectors on 50 μm center-to-center spacings had a 100% yield with leakage currents of <20 nA at −1 V and an average EQE of 73 ± 2%. Similarly, a square array was transferred onto a *rigid* Si substrate, resulting in a 99% yield with this same range of low-leakage currents (Supplementary Figure S2). The photodiode array was subjected to a burn-in test at 100 °C for 240 h. Both dark current and EQE at λ = 1550 nm at −1 V are measured (see Methods) at various intervals throughout the process. The normalized experimental results, showing the change of performance during burn-in, are almost constant within the 5% measurement error, as shown in Figure 3B. Also the performance of the array was tested before and after bending over radii ranging from 9.1 to 2.5 mm. Figure 3C shows the normalized dark current and EQE at λ = 1550 nm at −1 V following bending such that the upper half of the InGaAs active material was subjected to tensile stress and the lower half was subjected to compressive stress. No systematic performance changes are observed after bending.

Application 1: 2π Imager. Two applications were explored that benefit from the flexibility and/or conformability of the 2D detector array that can be sharply curved into either a concave or convex format without damage. The first is in creating 2π object awareness. For this application, the 8 × 100 photodiode array was wrapped into a convex, 1 cm diameter cylindrical shape to achieve a 360° (i.e., 2π) in-plane FOV, as shown in Figure 2A. To demonstrate this application, a 5 mW, 1550 nm wavelength laser beam is guided through an optical fiber with a numerical aperture of 0.14 to illuminate the photodiode array as it is rotated through 360°, pausing every 36° to collect an image. Assuming a Gaussian beam profile at the fiber output, a beam waist diameter of 10.4 ± 0.8 μm, and a 2.0 ± 0.1 cm distance from the fiber to the array, the calculated beam diameter at the array is 580 ± 25 μm. The measured beam diameter at the array surface at which the intensity drops to $1/e^2$ of its peak spans two pixels, which is consistent with the calculated result. As shown in Figure 4A, 10 laser output profiles are mapped to demonstrate 2π awareness. The peak-to-peak photocurrent variations of the 10 output profiles in Figure 4A are possibly due to instabilities in laser output power and optical alignment. Figure 4B shows the detected laser signal and the FOV covered by the array in both longitudinal and

DOI: 10.1021/acsphotonics.6b00042
ACS Photonics 2016, 3, 670−676

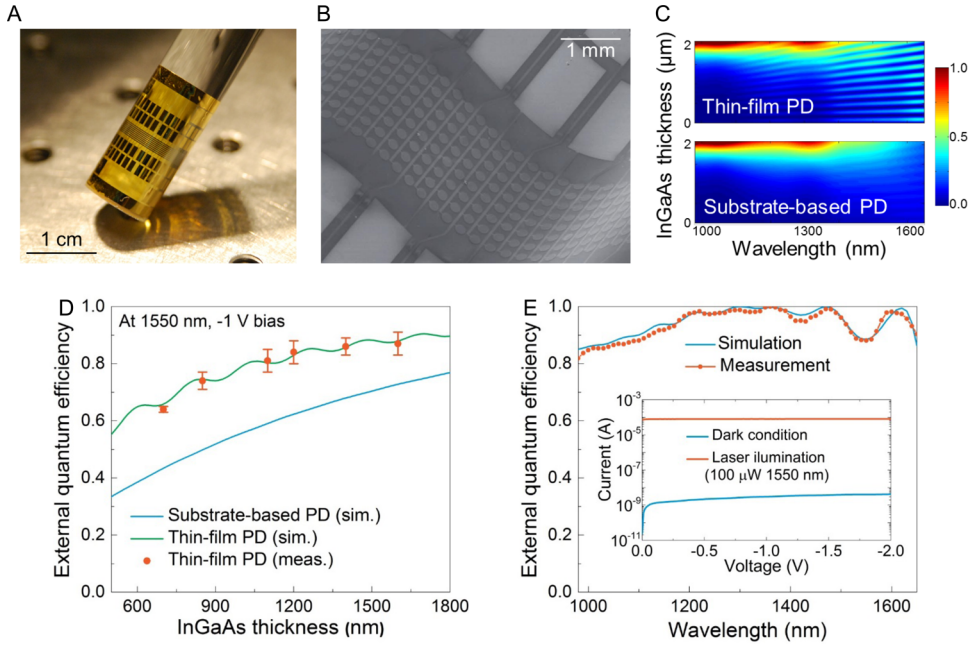

Figure 2. (A) Photograph of an 8 × 100 thin-film InGaAs p-i-n photodiode array fabricated on flexible Kapton foil. (B) Scanning electron microscopic image of the curved photodiode array. (C) Normalized simulated optical intensity distribution within the 2.1 μm thick InGaAs active region. A bilayer antireflection coating (ARC) of MgF_2 (37 nm) and TiO_2 (127 nm) is employed for both simulated structures. (D) Comparison of simulated and measured external quantum efficiencies (EQE) vs i-region thickness at −1 V bias and 1550 nm wavelength for thin-film (green line) and substrate-based devices (blue line). Measurements for photodiodes using a bilayer ARC of MgF_2 (81 nm) and TiO_2 (113 nm) are shown (data points). (E) Simulated (blue line) and measured (orange dots) EQE spectra of the photodiode in the wavelength range from 980 to 1650 nm. Inset: Current−voltage (I−V) characteristics of a 40 μm diameter photodiode in the dark (blue line) and under 100 μW, 1550 nm wavelength illumination (green line).

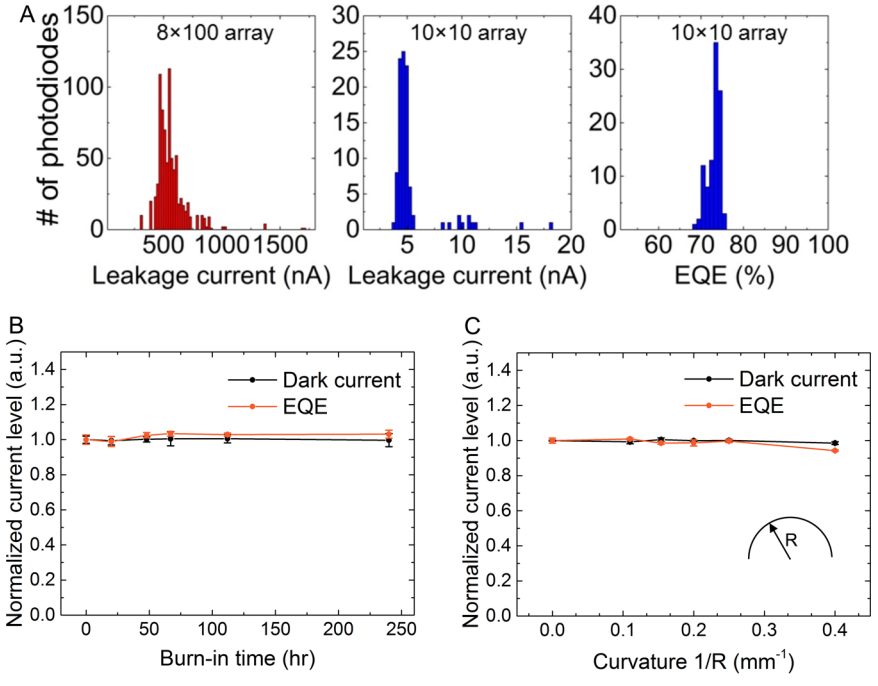

Figure 3. (A) Histograms of dark current of detectors on the (left) 8 × 100 and (middle) 10 × 10 FPAs. Also shown (right) is a histogram of the external quantum efficiencies of diodes on the 10 × 10 thin-film FPA. These graphs indicate a ∼99% device yield. (B) Change in normalized dark current and EQE under 100 °C burn-in test over 240 h measured at 0, 20, 48, 67, 112, and 240 h. (C) Change in normalized dark current and EQE under different bending conditions (radius of curvature of infinity (flat), 9.1 mm, 6.5 mm, 5 mm, 4 mm, and 2.5 mm). No systematic performance change is observed in either test.

latitudinal directions. Objects with arbitrary shapes can also be imaged, as shown in Supplementary Figure S4.

Application 2: High-Resolution Spectroscopy. The second application is in high-resolution spectroscopy. In a

DOI: 10.1021/acsphotonics.6b00042
ACS Photonics 2016, 3, 670−676

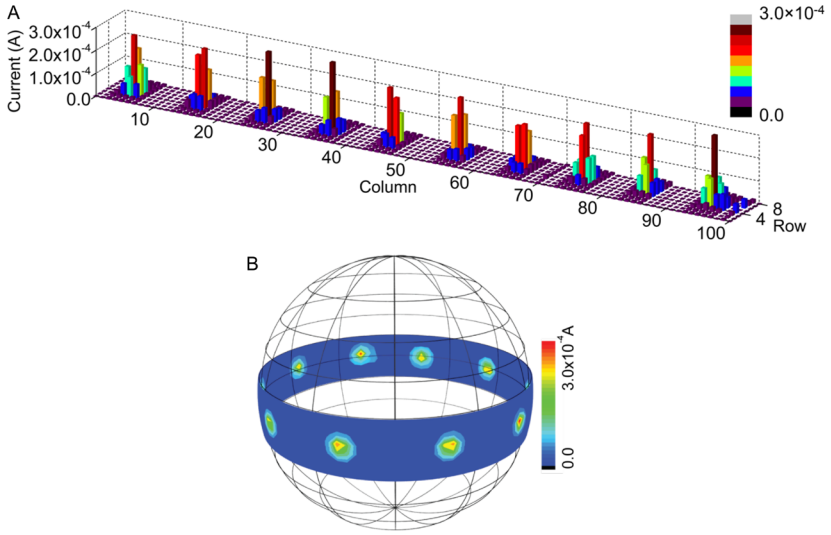

Figure 4. (A) Photocurrent map of laser output profiles on a convex cylindrical 8 × 100 photodiode array. Ten laser output profiles are shown, separated by 36°, verifying its 360° field of view (FOV). (B) Photocurrent response and the FOV covered by the cylindrical focal plane array in both the longitudinal and latitudinal directions.

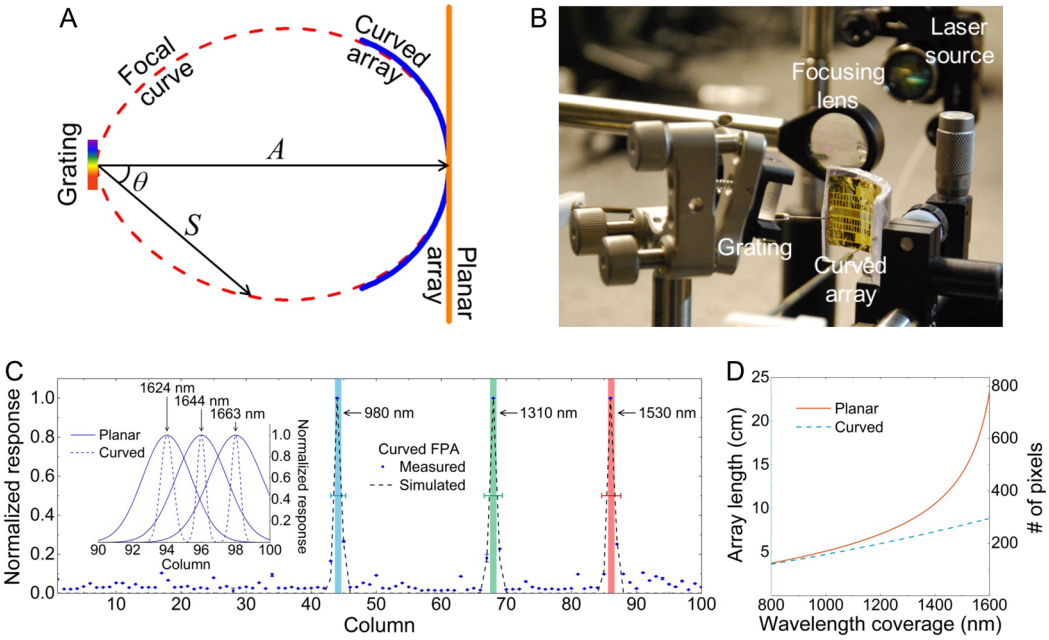

Figure 5. (A) Spectral focal plane (dashed line) following diffraction by a blaze grating (rainbow rectangle); the detector plane of the curved focal plane array (FPA) is shown by the blue arc whose shape matches the curvature of the focal plane. A planar FPA (orange line) is shown for comparison. (B) Photograph of the spectral measurement setup. Collimated laser beams are focused and diffracted onto the curved FPA. (C) Simulated (dashed line, assuming Gaussian beam profiles) and measured (data points) photocurrent response (normalized) of the cylindrically curved FPA. Also shown are the simulated one-pixel-width diffraction peak (vertical bars) positions at three different wavelengths of 980, 1310, and 1530 nm. Inset: Simulated response from pixels #90 to #100 on a cylindrical (dashed line) and a planar (solid line) FPA at three closely spaced wavelengths. (D) Comparison of the array length vs wavelength coverage required for a curved (dashed line) and a planar (solid line) FPA. The corresponding number of pixels required (right vertical axis) is also shown, assuming a pixel spacing of 300 μm. Note the dramatic divergence in array size as the wavelength span is increased.

Monk−Gillieson-type[27,28] spectrometer,[29] the distance, S, from a flat diffraction grating to the focal plane is given by[27]

$$S = A\cos^2\theta \tag{1}$$

where θ is the diffracted angle, $A = (f - D)/\cos^2\theta_i$, f is the focal length of the focusing component (a concave mirror or a lens), D is the distance from the focusing component to the grating, and θ_i is the light incident angle. Thus, A, depending on experimental arrangement, defines the distance from the grating to the *in-focus spectral line* as shown in Figure 5A. As $\theta \to 0$, $S \to A$, whereas as $\theta \to 90°$, $S \to 0$. This suggests that the spectral lines at large diffraction angles focus close to the grating rather than at the image plane. In contrast, a flexible FPA that is curved about an axis centered on the grating can be shaped to precisely match the focal region, maintaining focus independent of θ, as illustrated in Figure 5A. In this work, we shaped the FPA into a 2.54 cm diameter cylindrical curve (blue line, Figure 5A) to improve its match with the focal plane

DOI: 10.1021/acsphotonics.6b00042
ACS Photonics 2016, 3, 670−676

compared with that of a planar array (orange line, Figure 5A) to achieve higher spectral resolution at large diffracted angles.

The cylindrical 8 × 100 FPA was used to spatially resolve the outputs from three collimated laser beams at wavelengths of 980, 1310, and 1530 nm using the experimental arrangement in Figure 5B. The beams were shaped using air-spaced achromatic doublet collimators and a blaze reflective diffraction grating. Each laser beam was focused to a 300 ± 114 μm diameter spot, or approximately the pixel center-to-center spacing. Then, the response of the photodiodes was measured to locate the exact positions of each first-order diffraction maximum. Figure 5C shows the measured responses of the cylindrical FPA (data points), along with the simulated peak shapes (dashed lines, assuming Gaussian beam profiles) and positions (vertical, one-pixel-wide bars) of the diffracted wavelength signals. The measured peaks match the simulated results within the measurement error with no evidence for systematic broadening of the full width at half-maxima (fwhm). In Figure 5C, inset, we simulate the response near the imager edge (pixels #90 to #100) of both the cylindrical and a planar FPA. Closely spaced wavelengths of 1624, 1644, and 1663 nm (corresponding to diffraction angles of 28.32°, 29.10°, and 29.85° centered at pixels #94, #96, and #98, respectively) have 46.6%, 49.6%, and 53.3% mismatches between the focal distance, S, and the array-to-grating distances to the planar FPA, respectively. This corresponds to a greater than four pixel defocusing penalty, limiting the wavelength resolution to >44 nm. In contrast, mismatch between S and the array-to-grating distance of these same wavelengths to the cylindrical FPA are only 4.8%, 0.1%, and 0.5%, respectively, corresponding to a wavelength resolution smaller than 11 nm.

From Figure 5A, it is apparent that a curved FPA can provide a far wider spectral coverage than a planar FPA with the same number of pixels. That is, since each wavelength increment $\Delta\lambda$ subtends an angle $\Delta\theta$ about a central diffraction angle θ, the subtended linear increment Δl on a planar FPA is then

$$\frac{\Delta l}{A} \approx \sec^2 \theta \, \Delta\theta \tag{2}$$

Hence, Δl increases dramatically with $\Delta\theta$ in the limit of large θ. In contrast, the curved FPA follows

$$\frac{\Delta l}{A} \approx \Delta\theta \tag{3}$$

a function that is independent of diffraction angle θ. Figure 5D shows the wavelength coverage of both planar and curved FPAs using a 1200 grooves/mm diffraction grating. The array length required of an FPA curved to match the focal surface of the grating increases very slowly and approximately linearly with wavelength. Hence an 8.8 cm long array achieves coverage from 800 to 1600 nm, whereas the planar FPA length is dramatically increased 23.3 cm (see Supplementary Figure S6 for simulation details), with a correspondingly larger number of pixels.

A pixel spacing of 50 μm with a 40 μm mesa diameter was achieved using a manually aligned lithography tool with ~10 μm alignment tolerance. A smaller pixel spacing of <5 μm, which is orders of magnitude smaller than state-of-art conformal photodetector arrays,[6,9,7] are achievable using lithographic tools with higher resolution owing to the simplified ELO + precise cold-welding transfer methods that eliminate the brittle and significant bonding resolutions inherent in indium solder-bump technology. Additionally, transistor readout pixels can also be integrated with each photodiode in the array on the parent wafer and then transferred in a single step using the same fabrication methods as described here.[15]

CONCLUSION

In summary, we demonstrated a thin-film InGaAs p-i-n photodiode array fabricated on a thin, flexible Kapton foil substrate. The array is transformed into a cylindrical shape to achieve a 360° FOV to achieve 2π in-plane image awareness. The curved array was also used to improve focusing with enhanced wavelength coverage in a spectrophotometer application in comparison to a conventional planar array. Thin-film InGaAs photodiodes employing a back side mirror dramatically enhanced the detector responsivity by achieving EQE ≈ 100% over a wide SWIR spectral range. The unique features of this flexible and lightweight FPA enable advanced and simplified optical designs with exceptional FOV and significantly reduced aberrations, making it suitable for a wide variety of applications that cannot be accessed using planar arrays that are the foundation of modern imaging systems.

METHODS

Array Fabrication. Fabrication of the FPA (see Figure 1A) starts with the epitaxial growth of the InGaAs p-i-n photodiode active layer structure on a 2 in. (50.8 mm) diameter, Zn-doped (100) InP wafer using gas source molecular beam epitaxy. An undoped, 200 nm thick InP buffer layer is grown, followed by a 4 nm thick lattice-mismatched AlAs sacrificial layer, which is significantly greater than the critical thickness (~2 nm), above which a high density of defects is formed.[30] Nevertheless, transmission electron microscope images indicate no apparent defects in the epitaxial layers. Next, a 200 nm thick Be-doped (2×10^{18} cm^{-3}) p$^+$-InP window layer is grown, followed by a 2.1 μm thick unintentionally doped i-$In_{0.53}Ga_{0.47}As$ active absorption layer and a 100 nm thick Si-doped (5×10^{18} cm^{-3}) n$^+$-$In_{0.53}Ga_{0.47}As$ contact layer. The active device region is grown in inverted order such that top illumination p-i-n photodiode structures in Figure 1B result from bonding to the host (plastic) substrate and lift-off from the parent InP wafer.

The wafer is diced into 33 × 4 mm rectangles. Immediately after dicing, the epitaxial samples are rinsed with deionized water for 30 s to remove dicing residues. The samples are stored in acetone to prevent possible surface contamination from the environment. The samples are rinsed for 5 min in 2-propanol at 80 °C, and the surface native oxide of the epitaxial layer is removal in buffered HF for 1 min and rinsed in deionized (DI) water for 10 s. Next, 0.5 nm thick Ir followed by 200 nm thick Au layers are deposited by e-beam evaporation on both the epitaxial surface and a 25 μm thick, E-type Kapton host foil substrate. During deposition, the sample is taped to a 4 in. (101.6 mm) rigid Si handle to keep it flat, a method applied during all subsequent metal evaporation steps. The diced samples and host substrate are cold-weld bonded by applying heat (200 °C) and pressure (20 MPa) for 5 min under vacuum (10^{-4} mTorr) using an EVG 510 wafer bonder. To ensure the application of uniform force across the array during bonding, a soft graphite sheet is inserted between the sample and the bonder press head. The epitaxial layers are then separated from the parent InP substrate by removing the AlAs layer through immersion in 17% HF in water at 45 °C while agitating at 400 rpm using a magnetic stir bar. The epitaxial layers are fully transferred to the host substrate in 1.5 h. After ELO, the samples are stored at 60 °C in Remover PG

DOI: 10.1021/acsphotonics.6b00042
ACS Photonics 2016, 3, 670−676

(MicroChem) to prevent oxide formation on the epitaxial surface prior to further processing.

The Kapton substrate is attached to a 4 in. (101.6 mm) diameter rigid Si handle using Kapton tape to eliminate curling and wrinkling during device fabrication. All layers are photolithographically patterned using a LOR 3A (MicroChem) and S1827 (MicroChem) bilayer photoresist. A Ti (20 nm)/Pt (30 nm)/Au (200 nm) top ring contact (150 μm/170 μm inner/outer diameter) is deposited using e-beam evaporation and lifted off in Remover PG (MicroChem) to define the light detection area. Photodiode mesas (190 μm diameter, 314 μm pixel separation) are patterned using inductively coupled plasma (ICP) reactive-ion etching (RIE; Cl_2:H_2 = 16:12 sccm, 12 mTorr base pressure, 600 W ICP power, 100 W forward power, 0 °C stage temperature for 5 min). The back contact (100 μm width) is patterned using wet etching for 3 min in TFA Au etchant (Transene) to connect the photodiode rows. Ohmic contacts are formed by rapid thermal annealing for 1 min at 270 °C. A 1 μm thick polyimide (PI2610, HD Microsystem) passivation layer is spin-cast and cured at 300 °C for 30 min. The polyimide is patterned to expose the photodiode detection area and back contact pads using ICP RIE (O_2:CF_4 = 16:56 sccm, 5 mTorr base pressure, 500 W ICP power, 10 W forward power for 6 min). The e-beam-evaporated, 50 μm wide Ti (10 nm)/Au (300 nm) top contact is patterned to connect columns of photodiodes. Finally, a MgF_2 (37 nm)/TiO_2 (127 nm) bilayer antireflection coating is deposited by e-beam evaporation to achieve a maximum EQE at λ = 1300 nm.

Characterization. The current−voltage characteristics under dark and 100 μW 1550 nm laser illumination are measured using an HP-4155B semiconductor parameter analyzer. Illumination, from a tunable laser source (Santec TSL-510), is guided through an SMF-28 optical fiber oriented normal to the photodiode active area using a Lightwave Probe (Cascade Microtech). External quantum efficiency from wavelengths of 980 to 1650 nm is measured under monochromatic illumination chopped at 200 Hz and coupled into an SMF-28 optical fiber. The photocurrent at −1 V is amplified by 10^5 V/A using a Keithley 428 amplifier. The output signal is collected by a lock-in amplifier (SR830). The light illumination power is calibrated using a reference InGaAs photodetector (Newport, 818-IG/DB). Field of view and spectroscopic measurement details are provided in the Supporting Information.

■ ASSOCIATED CONTENT

Supporting Information

The Supporting Information is available free of charge on the ACS Publications website at DOI: 10.1021/acsphotonics.6b00042.

Further details related to the characterization, measurement, and simulation (PDF)

■ AUTHOR INFORMATION

Corresponding Author

*E-mail: stevefor@umich.edu.

Author Contributions

⊥D. Fan and K. Lee contributed equally to this work.

Author Contributions

D.F. and K.L. performed experiments and simulations; S.R.F. contributed to the experimental concepts and analysis.

Notes

The authors declare no competing financial interest.

■ ACKNOWLEDGMENTS

The authors thank Xiao Liu for assistance with device characterization, Xiaomi Zhang for assistance with sample preparation, and the Defense Advanced Research Projects Agency (DARPA) 4π-SCALE program and the Army Research Laboratory (ARL) MAST program for partial financial support. This work was performed in part at the Lurie Nanofabrication Facility, a member of the National Nanotechnology Infrastructure Network, which is supported in part by the National Science Foundation.

■ REFERENCES

(1) Rim, S.-B.; Catrysse, P. B.; Dinyari, R.; Huang, K.; Peumans, P. The Optical Advantages of Curved Focal Plane Arrays. *Opt. Express* **2008**, *16*, 4965.

(2) Swain, P. K.; Channin, D. J.; Taylor, G. C.; Lipp, S. A.; Mark, D. S. Curved CCDs and Their Application with Astronomical Telescopes and Stereo Panoramic Cameras. *Proc. SPIE* **2004**, 109−129.

(3) Brady, D. J.; Gehm, M. E.; Stack, R. A.; Marks, D. L.; Kittle, D. S.; Golish, D. R.; Vera, E. M.; Feller, S. D. Multiscale Gigapixel Photography. *Nature* **2012**, *486*, 386−389.

(4) Wong, W.; Salleo, A. *Flexible Electronics: Materials and Applications*; 2009.

(5) Yoon, J.; Lee, S.-M.; Kang, D.; Meitl, M. A.; Bower, C. A.; Rogers, J. A. Heterogeneously Integrated Optoelectronic Devices Enabled by Micro-Transfer Printing. *Adv. Opt. Mater.* **2015**, *3*, 1313−1335.

(6) Xu, X.; Davanco, M.; Qi, X.; Forrest, S. R. Direct Transfer Patterning on Three Dimensionally Deformed Surfaces at Micrometer Resolutions and Its Application to Hemispherical Focal Plane Detector Arrays. *Org. Electron.* **2008**, *9*, 1122−1127.

(7) Ko, H. C.; Stoykovich, M. P.; Song, J.; Malyarchuk, V.; Choi, W. M.; Yu, C.-J.; Geddes, J. B., III; Xiao, J.; Wang, S.; Huang, Y.; Rogers, J. A. A Hemispherical Electronic Eye Camera Based on Compressible Silicon Optoelectronics. *Nature* **2008**, *454*, 748−753.

(8) Saito, H.; Hoshino, K.; Matsumoto, K.; Shimoyama, I. *Compound Eye Shaped Flexible Organic Image Sensor with a Tunable Visual Field*; 18th IEEE International Conference on Micro Electro Mechanical Systems, 2005. MEMS 2005. IEEE, 2005; pp 96−99.

(9) Floreano, D.; Pericet-Camara, R.; Viollet, S.; Ruffier, F.; Brückner, A.; Leitel, R.; Buss, W.; Menouni, M.; Expert, F.; Juston, R.; Dobrzynski, M. K.; L'Eplattenier, G.; Recktenwald, F.; Mallot, H. A.; Franceschini, N. Miniature Curved Artificial Compound Eyes. *Proc. Natl. Acad. Sci. U. S. A.* **2013**, *110*, 9267−9272.

(10) Dinyari, R.; Rim, S.-B.; Huang, K.; Catrysse, P. B.; Peumans, P. Curving Monolithic Silicon for Nonplanar Focal Plane Array Applications. *Appl. Phys. Lett.* **2008**, *92*.16990110.1063/1.2908876

(11) Song, Y. M.; Xie, Y.; Malyarchuk, V.; Xiao, J.; Jung, I.; Choi, K.-J.; Liu, Z.; Park, H.; Lu, C.; Kim, R.-H.; Li, R.; Crozier, K. B.; Huang, Y.; Rogers, J. A. Digital Cameras with Designs Inspired by the Arthropod Eye. *Nature* **2013**, *497*, 95−99.

(12) Jin, H. C.; Abelson, J. R.; Erhardt, M. K.; Nuzzo, R. G. Soft Lithographic Fabrication of an Image Sensor Array on a Curved Substrate. *J. Vac. Sci. Technol., B: Microelectron. Process. Phenom.* **2004**, *22*.254810.1116/1.1795249

(13) Kim, C.; Burrows, P. E.; Forrest, S. R. Micropatterning of Organic Electronic Devices by Cold-Welding. *Science* **2000**, *288*, 831−833.

(14) Konagai, M.; Sugimoto, M.; Takahashi, K. High Efficiency GaAs Thin Film Solar Cells by Peeled Film Technology. *J. Cryst. Growth* **1978**, *45*, 277−280.

(15) Lee, K.; Zimmerman, J. D.; Hughes, T. W.; Forrest, S. R. Non-Destructive Wafer Recycling for Low-Cost Thin-Film Flexible Optoelectronics. *Adv. Funct. Mater.* **2014**, *24*, 4284−4291.

DOI: 10.1021/acsphotonics.6b00042
ACS Photonics 2016, 3, 670−676

(16) Rogalski, A. Progress in Focal Plane Array Technologies. *Prog. Quantum Electron.* **2012**, *36*, 342−473.
(17) Rogalski, A.; Antoszewski, J.; Faraone, L. Third-Generation Infrared Photodetector Arrays. *J. Appl. Phys.* **2009**, *105*, 09110110.1063/1.3099572.
(18) Coussement, J.; Rouvié, A.; Oubensaid, E. H.; Huet, O.; Hamard, S.; Truffer, J.-P.; Pozzi, M.; Maillart, P.; Reibel, Y.; Costard, E.; Billon-Lanfrey, D. New Developments on InGaAs Focal Plane Array. *Proc. SPIE* **2014**, 907005−907009.
(19) Wang, Y.-S.; Chang, S.-J.; Chiou, Y.-Z.; Lin, W. Noise Characteristics of High-Performance InGaAs PIN Photodiodes Prepared by MOCVD. *J. Electrochem. Soc.* **2008**, *155*, J307.
(20) Onat, B. M.; Huang, W.; Masaun, N.; Lange, M.; Ettenberg, M. H.; Dries, C. Ultra-Low Dark Current InGaAs Technology for Focal Plane Arrays for Low-Light Level Visible-Shortwave Infrared Imaging. *Proc. SPIE* **2007**, 65420L−9.
(21) Dowrey, A. E.; Story, G. M.; Marcott, C. Industrial Applications of Near-IR Imaging. In *Spectrochemical Analysis Using Infrared Multichannel Detectors*; Blackwell Publishing Ltd, 2005; pp 175−188.
(22) Blake, T.; Faccenda, W.; Lambour, R.; Shah, R.; Smith, A.; Gregory, J. G.; Pearce, E. C.; Woods, D.; Sundbeck, S.; Bolden, M. Utilization of a Curved Focal Surface Array in a 3.5m Wide Field of View Telescope *Proc. Adv. Maui Opt. Sp. Surveill. Technol. Conf.* 2013.
(23) Peumans, P.; Yakimov, A.; Forrest, S. R. Small Molecular Weight Organic Thin-Film Photodetectors and Solar Cells. *J. Appl. Phys.* **2003**, 93.369310.1063/1.1534621
(24) Martin, T.; Dixon, P.; Gagliardi, M.-A.; Masaun, N. 320 × 240 Pixel InGaAs/InP Focal Plane Array for Short-Wave Infrared and Visible Light Imaging. *Proc. SPIE* **2005**, 85−91.
(25) Martin, T.; Brubaker, R.; Dixon, P.; Gagliardi, M.-A.; Sudol, T. 640 × 512 InGaAs Focal Plane Array Camera for Visible and SWIR Imaging. *Proc. SPIE* **2005**, 12−20.
(26) Seshadri, S.; Cole, D. M.; Hancock, B.; Ringold, P.; Peay, C.; Wrigley, C.; Bonati, M.; Brown, M. G.; Schubnell, M.; Rahmer, G.; Guzman, D.; Figer, D.; Tarle, G.; Smith, R. M.; Bebek, C. Characterization of NIR InGaAs Imager Arrays for the JDEM SNAP Mission Concept. *Proc. SPIE* **2006**, 6276−8.
(27) Monk, G. S. A Mounting for the Plane Grating. *J. Opt. Soc. Am.* **1928**, *17*, 358−362.
(28) Gillieson, A. H. C. P. A New Spectrographic Diffraction Grating Mounting. *J. Sci. Instrum.* **1949**, *26*, 335.
(29) Kaneko, T.; Namioka, T.; Seya, M. Monk-Gillieson Monochromator. *Appl. Opt.* **1971**, *10*, 367−381.
(30) Matthews, J. W.; Blakeslee, A. E. Defects in Epitaxial Multilayers: I. Misfit Dislocations. *J. Cryst. Growth* **1974**, *27*, 118−125.

DOI: 10.1021/acsphotonics.6b00042
ACS Photonics 2016, 3, 670−676